






Bulk morphology of porous materials at submicrometer scale studied by dark-field x-ray imaging with Hartmann masks

Margarita Zakharova ^{1,2,*} Andrey Mikhaylov ¹ Stefan Reich ^{3,4} Anton Plech ³ and Danays Kunka ^{1,†}

¹*Institute of Microstructure Technology (IMT), Karlsruhe Institute of Technology (KIT), 76344 Eggenstein-Leopoldshafen, Germany*

²*Center for Free-Electron Laser Science (CFEL), Deutsches Elektronen-Synchrotron (DESY),*

Notkestraße 85, 22607 Hamburg, Germany

³*Institute of Photon Science and Synchrotron Radiation (IPS), Karlsruhe Institute of Technology (KIT),*

76344 Eggenstein-Leopoldshafen, Germany

⁴*Fraunhofer Institute for High-Speed Dynamics, Ernst Mach Institute (EMI), 79104 Freiburg, Germany*



(Received 21 August 2022; revised 17 September 2022; accepted 26 September 2022; published 18 October 2022)

We present the quantitative investigation of the submicron structure in the bulk of porous graphite by using the dark-field x-ray imaging with Hartmann masks. By scanning the correlation length and measuring the mask visibility reduction, we obtain the average pore size, relative pore fraction, fractal dimension, and Hurst exponent of the structure in a simple and flexible setup with relaxed requirements on beam coherence. Profiting from the dimensionality of the mask, we obtain scattering signals in two orthogonal directions, which reveals the anisotropy of pore sizes.

DOI: [10.1103/PhysRevB.106.144204](https://doi.org/10.1103/PhysRevB.106.144204)

I. INTRODUCTION

Porous materials are challenging objects for characterization: they typically exhibit a wide range of pore sizes, solid material opacity, possible anisotropy of the pores, and structure inhomogeneity in the bulk. Many conventional microscopic techniques have a limited field of view, which often makes the characterization they offer confined and incomprehensive. Excellent penetrating capabilities of x-ray radiation enable it to study otherwise opaque materials in a nondestructive way. Phase-contrast and dark-field x-ray imaging can offer a large field of view and provide different types of information retrieved from the projection of the sample (or a set thereof) [1–3].

Many x-ray imaging methods are based on the analysis of the changes in wave front modulation relative to a reference image [1–3]. The reference image records the initial wave front modulated by a chosen periodic optical element, such as a phase grating in grating-based interferometry [1,4], a speckle filter [5,6], a Fresnel zone plate [7], a lens array [8–10], or an x-ray absorption mask, including two-dimensional periodic arrays also reported as a Hartmann mask [11,12]. Being especially two-dimensional antigrids (pillar arrays), Hartmann masks facilitate wave front characterization, which can also be applied for characterizing the object under

investigation. This can be done by comparing the changes in the wave front with the so-called flat-field image with no object in the beam path. The disturbances in the wave front modulation introduced by a chosen object are analyzed and attributed to its properties. The general decrease in the intensity is related to transmission contrast, the shift of the modulation to the differential phase contrast, and the dampening of the projected modulation to the scattering contrast. The latter arises from an ultras-small-angle scattering of x rays on the fine inhomogeneities in the sample, and the phase signal below the resolution limit of the imaging setup [4,13,14].

The scattering signal (also commonly known as the dark field analogous to microscopy) can be evaluated in various ways, depending on the imaging method. The visibility reduction analysis is commonly used in grating-based x-ray interferometry, where the projected grating pattern is not directly resolved [1,4], and the stepping curve is analyzed to retrieve the decrease in visibility. This approach can also be applied in the case of the resolved projected pattern if the projected grating period is larger than the pixel size (here, we call them masks for distinction). Other approaches, which can be applied when the detector can resolve the mask period, include the broadening of an individual modulation peak [2,8] and the change in the first-order harmonic in the Fourier domain [3,13]. These methods offer an opportunity to probe structures at the sub- μm scale and retrieve information on their microscopic textural properties while performing macroscopic imaging.

Quantitative characterization of scattering contrast has been performed for surface analysis with x-ray grating interferometry with one-dimensional line gratings in a grazing-incidence configuration [15]. More recently, the volumetric porous samples were studied [16]; however, poor sampling

*margarita.zakharova@partner.kit.edu

†danays.kunka@kit.edu

and high noise of the retrieved dark-field signal did not allow for quantitative interpretation of the autocorrelation values.

Hartmann masks are essentially arrays of high-absorbing structures alternated by areas of high x-ray transmission. They can also be viewed as two-dimensional gratings with projected periods larger than the detector pixel size. The two main designs are an array of holes (conventional Hartmann mask) and an array of absorbing pillars (inverted Hartmann mask) [17]. Phase-contrast and dark-field x-ray imaging with Hartmann masks offers the advantages of setup robustness, relaxed requirements on the beam coherence, and versatility of the setup in the positioning of mask and sample. Hartmann masks can be fabricated by UV lithography combined with gold electroplating and scaled to the required field of view [18].

We used Hartmann masks of both designs to study the bulk morphology of porous graphite by analyzing the scattering contrast. Scattering contrast arises from the autocorrelation of electron density distribution, which peaks at a specific correlation length [19]. The specific probed peak correlation length ξ depends on the setup parameters [13,19,20]. For a fixed setup where the periodic optical element is placed before the object, it is defined as follows:

$$\xi = \frac{\lambda L}{P}, \quad (1)$$

where λ is the wavelength of the x-ray radiation, P is the period of the wave front modulation at the detector plane, and L is the distance from the object to the detector. By varying any of the values in Eq. (1), one can perform a scan of the correlation length and infer the autocorrelation function for the object under study [20–22].

Imaging with Hartmann masks has no restrictions on the positioning of the object; therefore, it provides fine scanning of the correlation length in the sub- μm range through the variation of L . By analyzing the visibility reduction, we can retrieve quantitative structural parameters of graphite using its real-space correlation function. This method can be applied to study textural properties of various complex microstructure systems, including *in situ* and *operando* measurements, and can be extended to laboratory setups.

II. THEORY

Visibility of the periodic modulation is a convolution of the modulation function and the scattering function. The modulation function is determined by the mask geometry and instrument resolution. When the visibility of the pattern decreases, it indicates stronger scattering by the object. The relationship between the decrease in visibility and the autocorrelation function of the electron density was defined elsewhere [23]. From this, we can determine the scattering intensity S as [4,21]

$$S = -\ln\left(\frac{V_\xi}{V_0}\right) = \sigma t[1 - G(\xi)], \quad (2)$$

where V_0 is the visibility of the projected mask pattern at no scattering ($\xi = 0$), V_ξ is the visibility of the projected mask pattern at the correlation length ξ , σ is the macroscopic scattering cross section, t is the sample thickness, and $G(\xi)$ is

the real-space autocorrelation function of electron density at the correlation length ξ [Eq. (1)].

The autocorrelation function depends on the structural properties of the object under study. For the dense but disordered structures such as graphite, the real-space autocorrelation function derived for random self-affine density distributions can be used [24–27],

$$G(\xi) = \frac{2}{\Gamma(H + 1/2)} \left(\frac{\xi}{2a}\right)^{H+1/2} K_{H+1/2}\left(\frac{\xi}{a}\right), \quad (3)$$

where a is the characteristic size parameter, $K_{H+1/2}(x)$ the modified Bessel function of the second kind of real order $(H + 1/2)$, and Γ the Gamma function. H is the so-called Hurst exponent ($0 < H < 1$) related to the dimensionality of the structure, namely to the interface roughness between the two phases of the material.

The Hurst exponent H from Eq. (3) is determined by the space-filling capacity of the structure and defines its fractal dimension $D = D_E + 1 - H$, where D_E is the Euclidean dimension of the scattering structure: 1 for filamentous, 2 for sheetlike, and 3 for bulk scatterers [27,28]. From this relation, one can see that the value of the Hurst exponent reflects the fractal dimension of the structure. The value of the Hurst exponent also describes the interconnection between the pores and the specific surface area of porous material. Two domains are usually discussed: $H > 1/2$, indicating that the density distribution is persistent (long-range correlations) with smoother and more interconnected pores, and $H < 1/2$, which corresponds to antipersistent distributions with smaller and more confined pores and low permeability [29]. The characteristic size of the structure d for random two-phase media can be understood as the average pore size and is derived from the size parameter a and the Hurst exponent H as follows [26]:

$$d = \frac{2\sqrt{\pi}a\Gamma(H + 1/2)}{\Gamma(H)}. \quad (4)$$

In our work, we also applied a simplified phenomenological fitting function [25,30] for the analysis of the pore size anisotropy

$$G(\xi) = \exp\left[-\left(\frac{\xi}{d}\right)^\alpha\right], \quad (5)$$

where $\alpha = D_E/2 + H$. Since $0 < H < 1$, the allowed range of values for α will depend on the Hurst exponent and the Euclidean dimension [24,27]. The allowed ranges of α will lie in the bounds $0.5 < \alpha_1 < 1.5$, $1 < \alpha_2 < 2$, and $1.5 < \alpha_3 < 2.5$ [27] for $D_E = (1, 2, 3)$, respectively. The value of α is related to the phase boundary and interface roughness [25,30,31].

III. EXPERIMENTAL DETAILS

A. Hartmann mask fabrication on graphite

Scattering contrast is usually determined through the decrease in the visibility of the projected mask pattern. This small-angle scattering-induced blurring is a relatively weak

signal, which can be mixed with setup-specific blurring due to the detector response and source characteristics. Thus, it is not possible to decipher quantitative values in the absolute single-distance measurement and requires high initial mask visibility to distinguish it from noise. To ensure the increased visibility of the mask pattern, minimize possible noise, and demonstrate the capabilities of the method, we fabricated Hartmann masks directly on the porous material. Nevertheless, such measurements can also be performed with a setup where the Hartmann mask is manufactured on a separate low-absorbing wafer, for example, polyimide [32], although extra care should be taken to eliminate the input from the substrate to the signal.

The wafers purchased from Ohio Carbon Blank, Inc., were synthetic graphite labeled “angstrofine” with a porous structure and an average grain size of $1\ \mu\text{m}$ as reported by the supplier (supplier identifier EDM-AF5). The separate wafers with a 4-inch diameter were cut out of the large graphite plate. Subsequently, the wafers were polished on both sides and rinsed in isopropanol. The final thickness of the wafers after processing was $500\ \mu\text{m}$.

The apparent density of the EDM-AF grade graphite material is reported to be $1.8\ \text{g}/\text{cm}^3$. Since the apparent density measurements include the pore volume in the calculation and the theoretical density of graphite is $2.26\ \text{g}/\text{cm}^3$, the pore fraction of graphite is at least 20%. The average pore size for the graphite with an apparent density of $1.8\ \text{g}/\text{cm}^3$ is $750 \pm 150\ \text{nm}$, as observed by mercury porosimetry [33]. The distribution of pore sizes for EDM-AF grade graphite is narrow compared to conventional graphite, with reported nominal pore size rating from 0.2 to $0.8\ \mu\text{m}$ [33].

The Hartmann masks were manufactured in a cleanroom environment using UV lithography, gold electroplating, and resist stripping [17]. Inverted and conventional Hartmann masks of various periods (30 , 40 , 60 , and $80\ \mu\text{m}$) with the gold height of about $30\ \mu\text{m}$ have been fabricated on the same substrate [34]. Additionally, a large-area ($5\ \text{cm} \times 5\ \text{cm}$) inverted Hartmann mask was produced on a different wafer from the same graphite plate. The masks will be further referred to as “mask type–period”, e.g., iHM-30 for the inverted Hartmann mask of period $30\ \mu\text{m}$ and HM-30 for conventional Hartmann mask of period $30\ \mu\text{m}$.

Based on a set of SEM images [Figs. 1(a), 1(b)], we performed surface pore size analysis. We identified the pores on the images by thresholding. Then, we estimated their Feret diameter (the longest distance between any two points along the selection boundary) to obtain the pore size distribution histogram [Fig. 1(c)]. The histogram follows a log-normal distribution with the peak at $550\ \text{nm}$. One can see that more than 60% of the pores are below $800\ \text{nm}$, which is in agreement with the nominal pore size rating reported for graphite wafers of EDM-AF grade [33].

B. Experimental setup

Visibility measurements have been carried out at the IPS imaging cluster of the KIT synchrotron facility [35]. After passing through beam-shaping slits, a Be window, and a double-multilayer monochromator, a quasi-monochromatic beam with an energy of $17\ \text{keV}$ and an energy bandwidth of 2% was incident on a Hartmann mask and graphite wafer

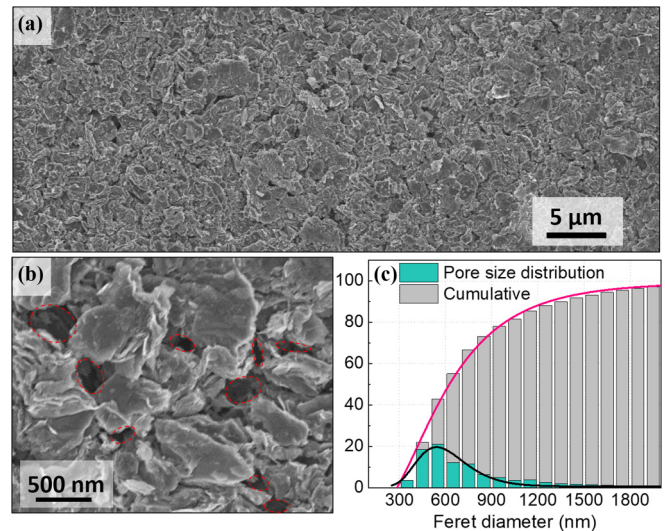


FIG. 1. The surface structure of graphite: SEM image of graphite surface (a) with a close-up view (b) outlining the pores in red; (c) surface pore size distributions histogram (green) and cumulative pore number (gray) versus Feret diameter based on the SEM image analysis.

behind it. Detection of the x-rays was performed by an Andor Neo 5.5 camera imaging an x-ray scintillator (LuAG) by lens coupling (magnification of 2.73) to achieve an effective pixel size of $2.4\ \mu\text{m}$. Detector size 2568×2161 pixels enabled the field of view of about $6\ \text{mm} \times 5\ \text{mm}$. The beam size at the sample was about $15\ \text{mm}$ (horizontal) \times $5\ \text{mm}$ (vertical), thus substantially covering the field of view of the detector ($6.16\ \text{mm} \times 5.2\ \text{mm}$). However, as the beam has a Gaussian shape, the intensity decreased toward the edge of the detector in the vertical direction. Due to this, we have used a cropped area of the projection, accounting for about $4.2\ \text{mm} \times 3.4\ \text{mm}$. The cropped areas slightly varied (within $60\ \mu\text{m}$) in order to accommodate the integer amount of unit cells of the mask. For Fourier analysis, the analyzed projections were cropped to a square, resulting in area of $3.4\ \text{mm} \times 3.4\ \text{mm}$ on average.

The experimental setup is shown in Fig. 2. For masks of 40 , 60 , and $80\ \mu\text{m}$ periods, sets of measurements for each mask separately were conducted. For different masks, the field of view was adjusted simply by moving the graphite wafer laterally (in X - Y planes) to a position of the mask, enabling identical imaging conditions for different masks. After placing the beam on the mask of interest, mask projections at different mask-detector distances were recorded, profiting from a linear stage movement range of $300\ \text{mm}$. In this way, we obtained the dependence of visibility on the position of the mask (distance to the detector). For the iHM of $50\ \mu\text{m}$ period, the measurements were performed in identical beam conditions, only by exchanging the graphite wafer on which the mask was manufactured. The masks were moved from $95\ \text{mm}$ to $395\ \text{mm}$ to the detector in 30 steps (step size $10\ \text{mm}$). An additional projection of the iHM-50 at a distance of $1120\ \text{mm}$ from the detector was acquired.

The changes in the visibility were attributed to the ultras-small-angle scattering in graphite, which was analyzed using the autocorrelation function for a random

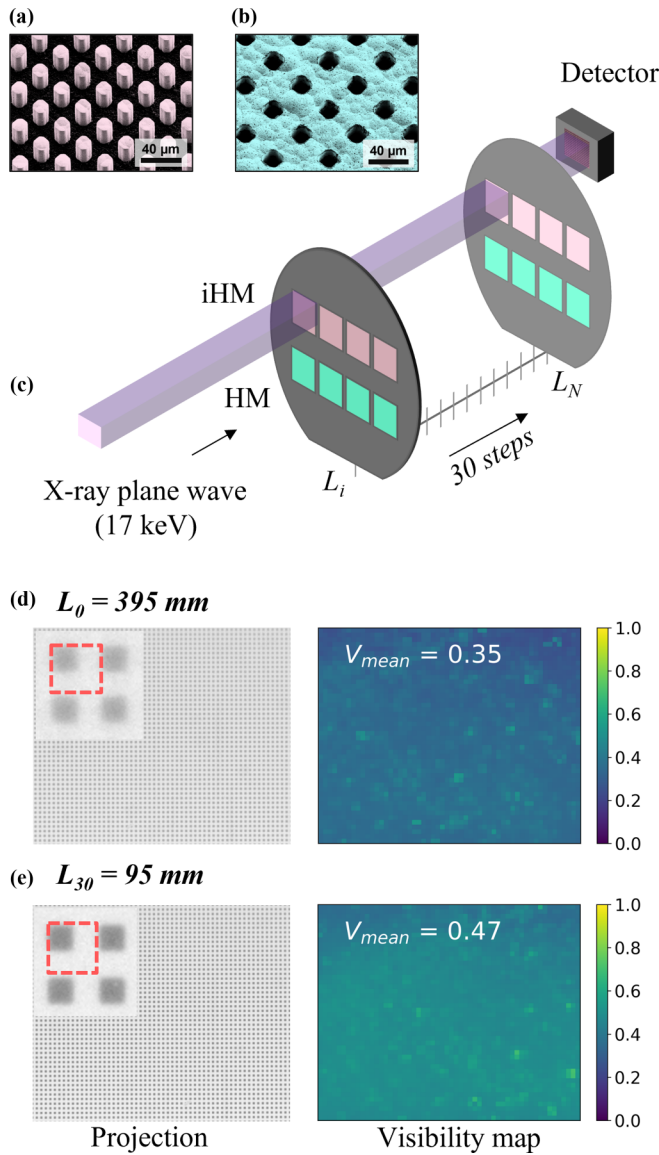


FIG. 2. Experimental setup for visibility measurements (c) with examples of patterns for inverted and conventional Hartmann masks in (a) and (b), respectively. Monochromatic x rays were incident on the mask, which was moving toward the detector with steps of 10 mm. The measurements were done with inverted and conventional Hartmann masks of different periods produced on porous graphite. For each step, a projection was recorded from which the visibility map was plotted: (d) and (e) show the projections and visibility maps for distances of 395 and 95 mm. Note how the mask projection gets sharper at shorter mask-detector distances [see the inset in (d) and (e)]; the dashed red square shows the unit cell of the mask]. The Supplemental Material contains detailed information on setup conditions and mask period sampling [34].

inhomogeneous two-phase media according to Eq. (3). The instrument resolution (source size) was much higher than the mask period; therefore, the change of the modulation function with distance is neglected [34]. The measurement conditions (e.g., detector, beam conditions, and stage) were identical; thus, the change in visibility was entirely attributed to the sample properties.

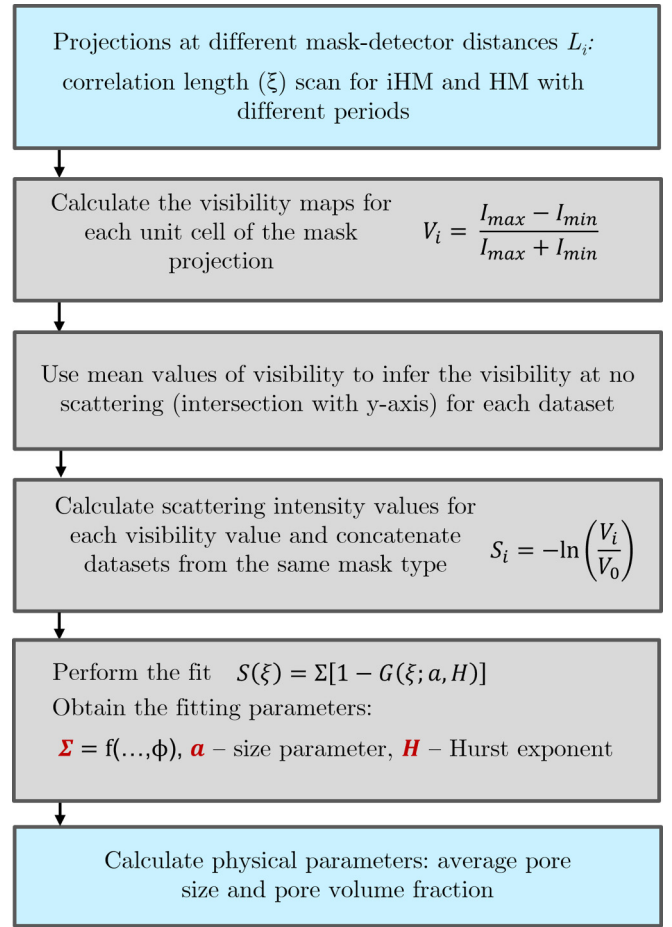


FIG. 3. Visibility reduction analysis scheme. The set of projections acquired at different distances to the detector was recorded for each mask. Then, for each unit cell of the mask, the value of visibility was calculated, taking local intensity minimum and maximum. The mean values V_i and standard deviations of visibility maps were then plotted for respective correlation lengths ξ_i in order to infer the value of visibility at no scattering V_0 . These values were then used to calculate the scattering intensity and obtain the structural parameters from the fit.

IV. DARK-FIELD INTENSITY ANALYSIS

A. Visibility reduction

Visibility reduction analysis was conducted as outlined in Fig. 3. The set of projections acquired at different distances to the detector was recorded for each mask. Then, for each unit cell of the mask (region of projected mask period), the value of visibility was calculated taking local intensity minimum I_{\min} and maximum I_{\max} as follows:

$$V = \frac{I_{\max} - I_{\min}}{I_{\max} + I_{\min}}, \quad (6)$$

where I_{\max} is the maximum and I_{\min} the minimum intensity within a beamlet zone.

The raw projections were cropped to the central area of the detector, where the illumination was homogeneous. Mean visibilities were calculated as mean values of the visibility maps in the analyzed area. In Figs. 4(a) and 4(b), the mean values of the visibility maps are plotted for the different masks

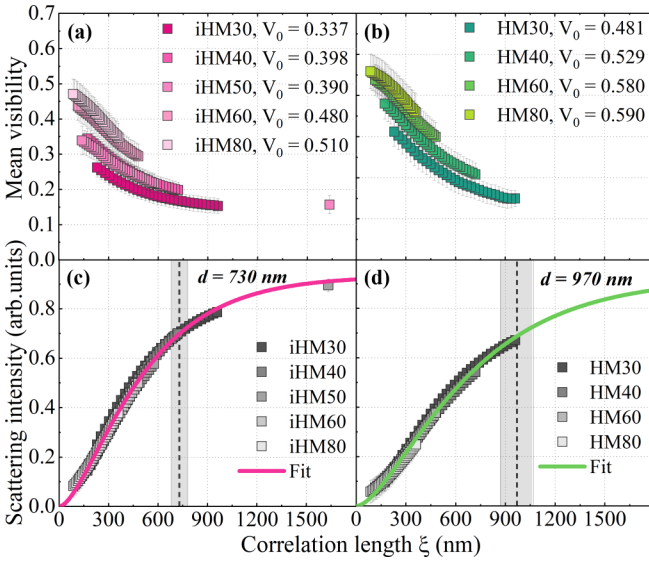


FIG. 4. Mean visibilities [(a), (b)] and scattering intensities [(c), (d)] [Eq. (2)] for (a), (c) inverted and (b), (d) conventional Hartmann masks on graphite, obtained for correlation lengths ξ scanned in the experiment. The error bars are the standard deviations of the obtained signal.

with error bars representing the standard deviation. The mean visibility values were then plotted for respective correlation lengths ξ_i . Under parallel beam geometry, the visibility decreases as the correlation length value gets larger due to the dampening of the mask contrast at the larger mask-to-detector distances.

To determine the scattering intensity [Eq. (2)] we need to know the mean visibility V_0 at no scattering such that $\xi = 0$ (equivalent to the mean of the modulation function). In a typical imaging setting, this would be the visibility of the reference image without the object. In our case, to determine V_0 we used the set of mean visibility V_i for each mask acquired at different correlation lengths ξ_i with $i = 1, 2, \dots, 30$. We performed a fit for the mean visibility values normalized by visibility at the smallest probed scattering length ξ_{\min} for each mask according to

$$\frac{V_i}{V_{\xi_{\min}}} = \exp\{\sigma t[G(\xi_i) - G(\xi_{\min})]\}, \quad (7)$$

where $G(\xi)$ is the projection of autocorrelation function at the correlation length ξ [Eq. (3)]. The obtained fitting parameters were plugged into the following equation,

$$V_0 = \frac{V_{\xi_i}}{\exp\{\sigma t[G(\xi_i) - 1]\}}, \quad (8)$$

to obtain the mean visibility values at no scattering V_0 for each mask, which are depicted in Figs. 4(a) and 4(b). These values were then used to obtain the scattering intensity S_i and we concatenated the data sets for different mask periods. In this way, fine sampling of the scattering intensity from 90 to 980 nm was achieved, which allowed for fitting using the autocorrelation function of electron density for dense disordered structure and retrieval of structural parameters with high precision.

The fit was performed using Eq. (2) and Eq. (3), and the fitting parameters σt , a , H were obtained. To check whether the fit correctly predicts the value of scattering intensity at correlation lengths larger than $1 \mu\text{m}$, we used the projection image for iHM-50 at the distance of 1120 mm from the detector, corresponding to the correlation length $\xi = 1.6 \mu\text{m}$. Note that the extra point acquired for the iHM-50 represents 1% of the data, and its influence on the fitting function can be neglected. As shown in Fig. 4(c), the value of the extra data point is well predicted by the fitting function.

The average pore size d was calculated as a function of the parameters a and H according to Eq. (4). The relative pore fraction ϕ_p under the spherical pore assumption can be calculated using the total scattering cross section σt according to the equation [19,26]

$$\sigma t = \frac{3\pi^2}{\lambda^2} d |\Delta\chi|^2 \phi_p \phi_s t, \quad (9)$$

where $|\Delta\chi|$ is the difference in complex refractive index between graphite and air, d is the average pore size, ϕ_s is a relative fraction of solid graphite, and t is the sample thickness. From the calculations for both mask types, we obtained the value of pore volume fraction $\phi_p = 22\%$. The parameters obtained from the fit and the calculated values of the average pore size and the relative pore fractions are presented in Table I.

An important parameter for porous material is its fractal dimension, which indicates how the pores are structured under fractal theory approximation [29,36]. The fractal dimension is defined by its Euclidean dimension D_E as well as the value of the Hurst exponent. Knowing that the phase boundary parameter α can be determined as $\alpha = H + D_E/2$, we can define the Euclidean dimension of the pore structure in graphite by performing a simplified fit according to Eq. (5) on the same data set. The fitting result indicated $\alpha = 1.46 \pm 0.02$ for iHM and $\alpha = 1.52 \pm 0.03$ for HM. From this, we can estimate the Euclidean dimension of the scatterers to be $D_E = 2$. The fractal dimension then is $D = D_E + 1 - H \approx 2.48 \pm 0.06$, attributed to fractal structures like Apollonian sphere packing ($D = 2.4739465$ [37]).

One can see from Table I that the error in fit parameters a and H , which are used to calculate the average pore size d [Eq. (4)], for inverted Hartmann masks is noticeably lower than that for the conventional Hartmann masks. The error for average pore size Δd was calculated as the error of indirect measurements using partial derivatives of Eq. (4) (Table I). The higher Δd might be caused by the fact that the area of the inverted Hartmann mask covered with gold is 25% of the total field of view of the sample; hence the scattering signal is formed from a larger object area compared to the conventional Hartmann mask. The total amount of scattering centers contributing to the signal is larger, making the obtained results more representative of the bulk structure. The advantage of having a higher signal-to-noise ratio when using the inverted Hartmann mask design for differential phase contrast imaging has been reported before [17].

The obtained values of average pore size and Hurst exponent can help to predict the pore size distribution. Practically

TABLE I. Parameters derived from the visibility measurements. Macroscopic cross section σt , characteristic parameter a , and Hurst exponent H are determined from the fit of experimental data. Average pore size d and relative pore fraction ϕ_p were calculated using the values of a , H , and σt .

Mask type	σt	a (nm)	H	d (nm) [Eq. (4)]	ϕ_p [Eq. (9)]
iHM	0.93 ± 0.02	326 ± 15	0.58 ± 0.05	730 ± 50	$22.5 \pm 0.4\%$
HM	0.92 ± 0.03	437 ± 32	0.58 ± 0.06	970 ± 100	$22.1 \pm 0.6\%$

important information about the pore size distribution is the peak (mode) of the distribution that indicates the most represented pore size, average (mean) pore size, and the width of the distribution—the range which contains most of the pores.

If we assume that pore sizes X are following a log-normal distribution, the expected value of the $\ln(X)$ will be $\mu = \ln(d)$, with d being the median of the pore size distribution. This value we obtain as characteristic pore size d . In the case of log-normal distribution, the median equals a multiplicative mean, which is in agreement with the typical pore structuring: smaller pores cluster and form larger pores, such that the cluster size grows proportionally to the size of the individual pore.

The Hurst exponent characterizes the deviation of the electron density distribution from the mean value (or “roughness of the distribution”). If we assume it to serve as an estimate of the standard deviation of the random variable $\ln(X)$, the geometric standard deviation factor will be e^H . Using the values of average pore size d and Hurst exponent H , we can evaluate the pore size range containing 2/3 of all pores as the scatter intervals of the distribution from $d/e^H = 400$ nm to $d \times e^H = 1340$ nm. We can simulate the log-normal distribution of a random variable X based on the data obtained by the scattering contrast [Fig. 5(a)]. Therefore, the peak of the distribution of pore sizes X is

$$\text{Mode}|X| = \exp[\ln(d) - H^2] \approx 520 \text{ nm}. \quad (10)$$

In Fig. 5, we compare the simulated bulk pore size distribution to the surface pore size distribution obtained from the set of SEM images. Note that the distribution obtained from SEM

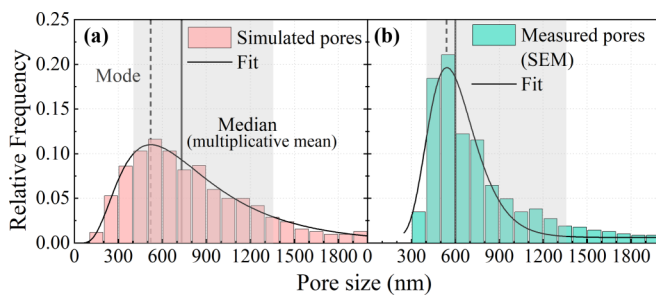


FIG. 5. Comparison of the pore size distributions: (a) simulated bulk pore size distribution based on the scattering data, (b) surface pore size distribution obtained from a set of SEM images. Modes of the distributions are indicated by the dashed lines and the medians by the solid lines. The gray-filled area represents the scatter intervals of the distributions containing 2/3 of all pores.

images is not comprehensive and is only valid for a restricted field of view (hence with limited pore size statistics) on the graphite surface. Nevertheless, it is a valuable benchmark to see if the simulated distribution is realistic. Figure 5 shows that, although the distributions differ in shape, the mode of the simulated distribution [dashed line at 520 nm in Fig. 5(a)] is close to the mode of the surface pore size distribution [shown as the dashed line at 540 nm in Fig. 5(b)]. The median of the simulated distribution (730 nm) is different from the median of the measured one (600 nm); we can see that the fit for the measured SEM distribution does not approximate the larger pores in the range from 900 nm to 1500 nm. Accounting for these pore clusters would make the distribution wider, shifting the median toward larger values.

B. Spatial harmonic analysis

One of the advantages of using the Hartmann mask is that it offers periodic modulation in two directions, which enables the separation of the horizontal and vertical components of the scattering signal. The visibility map analysis, while being easy and fast to implement, does not provide directional information about the scattering function [1,4]. To profit from that, we applied discrete Fourier transform to analyze the spatial beam modulation provided by the mask, as reported elsewhere [3,13].

The spatial frequency spectrum of the Hartmann mask projection contains a strong primary peak around zero spatial frequency and several sharp peaks separated by the $2\pi/P$ distance, where P is the period of the mask. In such a setting, S_{01} and S_{10} are attributed to scattering intensities in the horizontal and vertical directions, respectively. The scattering signals S_{01} or S_{10} are obtained from the first-order spatial harmonics and are linearized to the thickness of the sample as follows:

$$S_{mn} = -\ln \left[\frac{\mathcal{F}^{-1}\{I_{mn}\}/\mathcal{F}^{-1}(I_{mn}^{ref})}{T} \right], \quad (11)$$

where mn are equal to (01) or (10) for horizontal and vertical directions, respectively, \mathcal{F}^{-1} denotes the inverse fast Fourier transform of the spatial harmonic I_{mn} or I_{mn}^{ref} for reference projection, in this case, either I_{01} or I_{10} , and T is the transmission of the sample, obtained from the decrease of the zeroth harmonic. As we did not obtain a scattering-free reference image in our measurements (the mask was manufactured directly on the graphite), we used the projection at the shortest mask-detector distance as a reference image. This

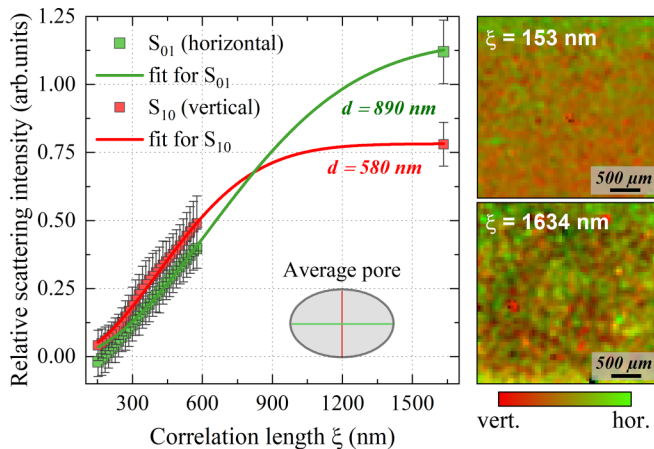


FIG. 6. Directional analysis of scattering contrast is represented by an overlay of the Fourier amplitudes S_{01} in horizontal (green) and S_{10} in vertical direction (red) for iHM50. The two-dimensional scattering intensity distribution maps for correlation lengths $\xi = 153$ nm and $\xi = 1634$ nm are shown on the right as pseudocolor images. The inset in the graph shows the shape of an average pore.

means that we analyzed only the change in scattering intensity relative to the signal at the smallest correlation length. Another consequence of this limitation is that we cannot concatenate data sets to achieve fine sampling over the whole range of correlation lengths probed with visibility analysis. For that reason, we chose the iHM50 mask, which was imaged at a long mask-detector distance, and thus can provide information on scattering intensities at larger correlation lengths.

Since S_{01} and S_{10} are defined for each effective pixel of the imaging system, we obtained the scattering distribution maps in two dimensions for each correlation length ξ . Examples of such maps for correlation lengths $\xi = 153$ nm and $\xi = 1634$ nm are shown in Fig. 6. One can see the directional distribution of scatterers in horizontal (green) and vertical (red) directions through the non-even distribution of red and green in the pseudocolor images. The mean values of S_{01} and S_{10} for different correlation lengths represented by the data points show that the scattering is mostly isotropic for pores smaller than 580 nm. As the length scale increases up to 1600 nm, the horizontal scattering starts to dominate.

For the data in Fig. 6 we applied the simplified fit according to Eq. (5) with $1 < \alpha < 2$. We determined the characteristic pore size in horizontal and vertical directions to be $d_{\text{hor}} = 890 \pm 60$ nm and $d_{\text{vert}} = 580 \pm 20$ nm, and the average of the two being 735 nm, which is in agreement with the average pore size obtained by the visibility map analysis. The average pore size in the horizontal direction is larger than in the vertical, indicating the elliptical shape of the characteristic pores (Fig. 3). Note that relative scattering signal measurements cannot correctly predict the pore fraction and Hurst exponent.

Another limitation of such an approach is a strong dependence on the x-ray absorption cross section of the object. For thick or highly absorbing specimens, special care has to be taken to eliminate the impact of spurious signal coming from

the cross talk between the absorption and scattering channels [9,38]. For low-absorbing and thin graphite, this effect is not pronounced, as was confirmed by the negligible change in the zeroth-order harmonic intensity for projections acquired at different distances.

V. CONCLUSIONS

This paper studied the morphology of bulk pore structure in fine graphite with the scattering contrast available through multimodal x-ray imaging with Hartmann and inverted Hartmann masks. We scanned the correlation length to study the real-space autocorrelation function of electron density by analyzing the mask visibility reduction. Moreover, we observed the pore size anisotropy by evaluating the relative change in the first-order spatial harmonics using Fourier analysis.

Based on the presented results, we have determined the pore volume fraction $\phi_p = 22\%$ and the characteristic pore size $d = 730 \pm 50$ nm for measurements with inverted Hartmann masks and $d = 970 \pm 100$ nm for conventional Hartmann masks. Both pore fraction and the average pore size values are in close agreement with the values reported for “angstrofine” grade graphite [33].

In addition to the visibility reduction analysis, we have applied the spatial harmonic approach to discriminate between horizontal and vertical scattering relative intensities. The pore sizes obtained with this approach are in agreement with the values obtained with visibility reduction analysis and additionally indicate that the pores are likely to be elliptical.

Given that the Hurst exponent $H = 0.5$ is characteristic for a perfectly random inhomogeneous solid, the obtained $H = 0.58$ suggests that the distributions of inhomogeneities in graphite are predominantly random with a slight inclination to being persistent. The fractal dimension of $D = 2.48$ implies that the pore structure of graphite can be represented by the spheres of different size cotangent to each other [39]. Considering the obtained results and calculated errors, we note that the inverted Hartmann mask design may be beneficial for x-ray scattering measurements due to the larger interaction volume contributing to the contrast formation: for the inverted mask 75% of the illuminated sample volume contributes to the signal, while for the conventional mask it is only 25%. This implies that the scattering signal obtained with conventional Hartmann masks is weaker and more susceptible to noise. To get more reliable pore size values, we would recommend using an inverted Hartmann mask. However, as conventional Hartmann masks are essentially absorbing grids, they might be more readily available and easier to manufacture. For measurement with the conventional Hartmann masks, we would recommend either ensuring a high photon count or longer exposure time or displacing the mask over the unit cell in horizontal and vertical directions to provide a large sample volume that has contributed to the signal.

We see our approach as a valuable addition to complementary techniques such as microscopy and tomography. We hope to bridge and complement them with information about scattering structures ranging from tens of nanometers to

micrometers. We expect such a versatile and straightforward technique to impact research devoted to studying complex structures like porous materials, colloids [40], or powders. Apart from the immediate profit for the development and characterization of porous catalytic materials, numerous medical applications related to early-stage cancer diagnostics [27] and lung diseases [21,41] can profit from the information on morphology and fractal dimensions of complex interconnected structures.

ACKNOWLEDGMENTS

This work was carried out with the support of KIT light source KARA and Karlsruhe Nano Micro Facility (KNMF). The authors thank Marcus Zuber and Sabine Bremer for their help during the measurements. The authors acknowledge the funding of the Karlsruhe School of Optics and Photonics (KSOP), associated institution at KIT, and the Karlsruhe House of Young Scientists (KHYS).

-
- [1] F. Pfeiffer, T. Weitkamp, O. Bunk, and C. David, *Nat. Phys.* **2**, 258 (2006).
- [2] F. A. Vittoria, M. Endrizzi, P. C. Diemoz, A. Zamir, U. H. Wagner, C. Rau, I. K. Robinson, and A. Olivo, *Sci. Rep.* **5**, 16318 (2015).
- [3] H. H. Wen, E. E. Bennett, R. Kopace, A. F. Stein, and V. Pai, *Opt. Lett.* **35**, 1932 (2010).
- [4] W. Yashiro, Y. Terui, K. Kawabata, and A. Momose, *Opt. Express* **18**, 16890 (2010).
- [5] S. Berujon, H. Wang, and K. Sawhney, *Phys. Rev. A* **86**, 063813 (2012).
- [6] I. Zanette, T. Zhou, A. Burvall, U. Lundström, D. H. Larsson, M. Zdora, P. Thibault, F. Pfeiffer, and H. M. Hertz, *Phys. Rev. Lett.* **112**, 253903 (2014).
- [7] M. Kagias, Z. Wang, P. Villanueva-Perez, K. Jefimovs, and M. Stampanoni, *Phys. Rev. Lett.* **116**, 093902 (2016).
- [8] T. dos Santos Rolo, S. Reich, D. Karpov, S. Gasilov, D. Kunka, E. Fohtung, T. Baumbach, and A. Plech, *Appl. Sci.* **8**, 737 (2018).
- [9] S. Reich, T. dos Santos Rolo, A. Letzel, T. Baumbach, and A. Plech, *Appl. Phys. Lett.* **112**, 151903 (2018).
- [10] A. Mikhaylov, S. Reich, M. Zakharova, V. Vlnieska, R. Laptev, A. Plech, and D. Kunka, *J. Synchrotron Radiat.* **27**, 788 (2020).
- [11] M. Zakharova, S. Reich, A. Mikhaylov, V. Vlnieska, T. dos Santos Rolo, A. Plech, and D. Kunka, *Opt. Lett.* **44**, 2306 (2019).
- [12] A. Letzel, S. Reich, T. dos Santos Rolo, A. Kanitz, J. Hoppius, A. Rack, M. P. Olbinado, A. Ostendorf, B. Gökce, A. Plech *et al.*, *Langmuir* **35**, 3038 (2019).
- [13] H. Wen, E. E. Bennett, M. M. Hegedus, and S. C. Carroll, *IEEE Trans. Med. Imag.* **27**, 997 (2008).
- [14] T. Koenig, M. Zuber, B. Trimborn, T. Farago, P. Meyer, D. Kunka, F. Albrecht, S. Kreuer, T. Volk, M. Fiederle *et al.*, *Phys. Med. Biol.* **61**, 3427 (2016).
- [15] W. Yashiro, S. Ikeda, Y. Wada, K. Totsu, Y. Suzuki, and A. Takeuchi, *Sci. Rep.* **9**, 1 (2019).
- [16] B. K. Blykers, C. Organista, M. N. Boone, M. Kagias, F. Marone, M. Stampanoni, T. Bultreys, V. Cnudde, and J. Aelterman, *Sci. Rep.* **11**, 18446 (2021).
- [17] M. Zakharova, S. Reich, A. Mikhaylov, V. Vlnieska, M. Zuber, S. Engelhardt, T. Baumbach, and D. Kunka, in *EUV and X-Ray Optics: Synergy between Laboratory and Space VI*, Proc. SPIE, Vol. 11032 (International Society for Optics and Photonics, Bellingham, WA, 2019), p. 110320U.
- [18] M. Zakharova, V. Vlnieska, H. Fornasier, M. Börner, T. d. S. Rolo, J. Mohr, and D. Kunka, *Appl. Sci.* **8**, 468 (2018).
- [19] S. K. Lynch, V. Pai, J. Auxier, A. F. Stein, E. E. Bennett, C. K. Kemble, X. Xiao, W.-K. Lee, N. Y. Morgan, and H. H. Wen, *Appl. Opt.* **50**, 4310 (2011).
- [20] F. Prade, A. Yaroshenko, J. Herzen, and F. Pfeiffer, *Europhys. Lett.* **112**, 68002 (2015).
- [21] K. Taphorn, F. De Marco, J. Andrejewski, T. Sellerer, F. Pfeiffer, and J. Herzen, *Sci. Rep.* **10**, 13195 (2020).
- [22] M. Kagias, Z. Wang, G. Lovric, K. Jefimovs, and M. Stampanoni, *Phys. Rev. Appl.* **15**, 044038 (2021).
- [23] M. Strobl, *Sci. Rep.* **4**, 7243 (2014).
- [24] C. Sheppard, *Opt. Commun.* **122**, 178 (1996).
- [25] R. Andersson, L. F. Van Heijkamp, I. M. De Schepper, and W. G. Bouwman, *J. Appl. Cryst.* **41**, 868 (2008).
- [26] R. Andersson, W. Bouwman, S. Luding, and I. M. De Schepper, *Phys. Rev. E* **77**, 051303 (2008).
- [27] M. Hunter, V. Backman, G. Popescu, M. Kalashnikov, C. W. Boone, A. Wax, V. Gopal, K. Badizadegan, G. D. Stoner, and M. S. Feld, *Phys. Rev. Lett.* **97**, 138102 (2006).
- [28] R. F. Voss, in *Fundamental Algorithms for Computer Graphics*, edited by R. A. Earnshaw, NATO ASI Series Vol. 17 (Springer, Berlin, Heidelberg, 1985), pp. 805–835.
- [29] M. Prostedny, A. Fletcher, and P. Mulheran, *RSC Adv.* **9**, 20065 (2019).
- [30] S. K. Sinha, E. B. Sirota, S. Garoff, and H. B. Stanley, *Phys. Rev. B* **38**, 2297 (1988).
- [31] Y. I. Nesterets, *Opt. Commun.* **281**, 533 (2008).
- [32] F. Koch, T. Schröter, D. Kunka, P. Meyer, J. Meiser, A. Faisal, M. Khalil, L. Birnbacher, M. Viermetz, M. Walter *et al.*, *Rev. Sci. Instrum.* **86**, 126114 (2015).
- [33] Entegris, Inc, Graphite properties and characteristics, <https://poco.entegris.com/content/dam/poco/resources/reference-materials/brochures/brochure-graphite-properties-and-characteristics-11043.pdf> (2013).
- [34] See Supplemental Material at <http://link.aps.org/supplemental/10.1103/PhysRevB.106.144204> for more details on the experimental setup, the impact of blurring and beam divergence, as well as Hartmann masks specifications.
- [35] A. Rack, T. Weitkamp, S. B. Trabetsi, P. Modregger, A. Cecilia, T. dos Santos Rolo, T. Rack, D. Haas, R. Simon, R. Heldele *et al.*, *Nucl. Instrum. Methods Phys. Res. Sect. B* **267**, 1978 (2009).
- [36] P. Adler and J.-F. Thovert, *Transp. Porous Media* **13**, 41 (1993).
- [37] M. Borkovec, W. De Paris, and R. Peikert, *Fractals* **02**, 521 (1994).
- [38] S. Kaepler, F. Bayer, T. Weber, A. Maier, G. Anton, J. Hornegger, M. Beckmann, P. A. Fasching,

- A. Hartmann, F. Heindl *et al.*, in *International Conference on Medical Image Computing and Computer-Assisted Intervention* (Springer, Boston, MA, 2014), pp. 170–177.
- [39] J. S. Andrade Jr., H. J. Herrmann, R. F. S. Andrade, and L. R. da Silva, *Phys. Rev. Lett.* **94**, 018702 (2005).
- [40] F. Dallari, A. Jain, M. Sikorski, J. Möller, R. Bean, U. Boesenberg, L. Frenzel, C. Goy, J. Hallmann, Y. Kim *et al.*, *IUCrJ* **8**, 775 (2021).
- [41] M. Helmberger, M. Pienn, M. Urschler, P. Kullnig, R. Stollberger, G. Kovacs, A. Olschewski, H. Olschewski, and Z. Balint, *PLoS ONE* **9**, e87515 (2014).